Hybrid System of Unbonded Post-Tensioned CLT Panels and Light-Frame Wood Shear Walls

Tu Xuan Ho[1]; Thang Nguyen Dao, M.ASCE[2]; Sriram Aaleti, A.M.ASCE[3]; John W. van de Lindt, F.ASCE[4]; and Douglas R. Rammer, M.ASCE[5]

Abstract: Cross-laminated timber (CLT) is a relatively new type of massive timber system that has shown to possess excellent mechanical properties and structural behavior in building construction. When post-tensioned with high-strength tendons, CLT panels perform well under cyclic loadings because of two key characteristics: their rocking behavior and self-centering capacity. Although post-tensioned rocking CLT panels can carry heavy gravity loads, resist lateral loads, and self-center after a seismic event, they are heavy and form a pinched hysteresis, thereby limiting energy dissipation. Conversely, conventional light-frame wood shear walls (LiFS) provide a large amount of energy dissipation from fastener slip and, as their name implies, are lightweight, thereby reducing inertial forces during earthquakes. The combination of these different lateral behaviors can help improve the performance of buildings during strong ground shaking, but issues of deformation compatibility exist. This study presents the results of a numerical study to examine the behavior of post-tensioned CLT walls under cyclic loadings. A well-known 10-parameter model was applied to simulate the performance of a CLT-LiFS hybrid system. The post-tensioned CLT wall model was designed on the basis of a modified monolithic beam analogy that was originally developed for precast concrete-jointed ductile connections. Several tests on post-tensioned CLT panels and hybrid walls were implemented at the Large Scale Structural Lab at the University of Alabama to validate the numerical model, and the results showed very good agreement with the numerical model. Finally, incremental dynamic analysis on system level models was compared with conventional light-frame wood system models. **DOI: 10.1061/(ASCE)ST.1943-541X.0001665.** *© 2016 American Society of Civil Engineers.*

Author keywords: Cross-laminated timber (CLT); Post-tensioned; Light frame wood shear wall; Hybrid system; Cyclic loads; Incremental dynamic analysis (IDA); Wood structures.

Downloaded from ascelibrary.org by Thang Dao on 09/07/16. Copyright ASCE. For personal use only; all rights reserved.

Introduction

A light-frame wood building is comprised of several components or subassemblies, such as diaphragms, walls, floors, and roof systems connected by intercomponent connections, in which light-frame shear walls (LiFS) play an important role in providing both the vertical load-bearing capacity and the lateral force resistance for the building. In a shear wall, the high racking strength of the sheathing connected to the frame members by fasteners provides rigidity to resist lateral forces and minimize deflections, whereas the studs in the frames transfer gravity loads from the floors, roofs, and walls to the foundation. When racking, the slip of nails in the shear wall allows wood shear walls to dissipate energy effectively. However, the vertical load-bearing capacity of light-frame structures is lower than that of massive timber systems such as cross-laminated timber (CLT). Furthermore, after several recent earthquakes, significant structural and nonstructural damages were observed in light-frame wood buildings. For example, the 1994 Northridge earthquake in California resulted in an estimated property loss of $20 billion to light-frame wood construction (Kircher et al. 1997). Currently, light-frame wood structures have been used primarily for residential buildings and low-rise commercial buildings, with construction as high as six stories, but typically in the one-to-four story range.

CLT is a relatively new structural system first introduced in Europe in the early 1990s and categorized as a massive timber system in the International Building Code (ICC 2009). It shows relatively high in-plane and out-of-plane strength and stiffness properties, improved dimensional stability, excellent fire resistance, and satisfactory performance in thermal and sound insulation if implementing proper design and installation. This new construction was developed in Europe in the early 2000s, and has recently spread to North America, Japan, and New Zealand. It has been used in over 100 CLT-construction projects around the world (Gagnon et al. 2013). CLT allows constructing midrise and high-rise wood buildings, which is more difficult with light-frame. Increasing interest in CLT in North America has led to the publication of CLT handbook: Cross-Laminated Timber (Gagnon and Pirvu 2011); the American national standard, Standard for Performance Rated Cross-Laminated Timber (ANSI/APA PRG 320) developed by the ANSI/APA CLT Standard Committee (ANSI/APA 2012); and the U.S. CLT Handbook (Gagnon et al. 2013). In 2015, the National Design Specification for Wood Construction (AWC 2015) adopted CLT design provisions, the first design specification worldwide to do so. All these publications summarized the state-of-the-art understanding of CLT seismic behavior and identified the need to better understand the seismic behavior of CLT structures.

[1]Ph.D. Candidate, Dept. of Civil, Construction, and Environmental Engineering, Univ. of Alabama, Tuscaloosa, AL 35487-0205.

[2]Assistant Professor, Dept. of Civil, Construction, and Environmental Engineering, Univ. of Alabama, Tuscaloosa, AL 35487-0205 (corresponding author). E-mail: tndao@eng.ua.edu

[3]Assistant Professor, Dept. of Civil, Construction, and Environmental Engineering, Univ. of Alabama, Tuscaloosa, AL 35487-0205.

[4]George T. Abell Professor in Infrastructure, Dept. of Civil and Environmental Engineering, Colorado State Univ., Fort Collins, CO 80523-1372.

[5]Research General Engineer, Forest Products Laboratory, 1 Gifford Pinchot Dr., Madison, WI 53726-2398.

Note. This manuscript was submitted on February 20, 2016; approved on July 28, 2016; published online on September 7, 2016. Discussion period open until February 7, 2017; separate discussions must be submitted for individual papers. This paper is part of the ***Journal of Structural Engineering***, © ASCE, ISSN 0733-9445.

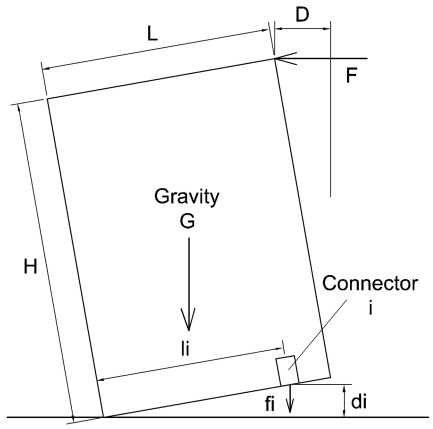

Fig. 1. Simplified kinematics model for CLT wall lateral resistance (data from Pei and van de Lindt 2011a)

Recently, an effective simplified model was developed by Pei and van de Lindt (2011a) that can be used to estimate the hysteresis of the CLT wall systems. In that study, there were several assumptions made regarding the load and the system behaviors, including: (1) CLT wall panels behave as in-plane rigid bodies; (2) under lateral loading, CLT wall panels will rotate individually around the bottom corners to develop lateral displacement at the top of the wall; (3) there is no relative lateral slip between the wall and floor (or ceiling) panels; (4) the gravity force acts vertically through the center of the CLT wall panels; and (5) panel connectors (for example: hold-downs and brackets) will be deformed during the rocking motion of the wall and develop the hysteresis of the wall panel system (Pei and van de Lindt 2011a).

These kinematic assumptions are shown in Fig. 1. On the basis of free body equilibrium, the lateral resistance of a CLT wall is presented as a scaled summation of the load-slip resistance of all the connectors engaged in the rocking movement of the wall. The scale factor for each connector is a function of their locations and the geometry of the panel. This model, combined with the calibrated connector hysteretic parameters, reasonably predicted accurate lateral response when compared with the FPInnovations experimental results (Popovski et al. 2010). However, it is applied only for a certain story drift level and short-wall panel length because of small angle approximation and the rotation assumption in the model (van de Lindt et al. 2013).

In general, the seismic performance of this rocking system relies on the inelastic behavior of materials (plastic deformations accepted within selected plastic hinge regions), the use of energy dissipation connections, and supplemental damping devices. These structural engineering techniques often are used in design to protect the structural system from undesired inelastic mechanisms and damage.

Recently, there have been several experimental and numerical studies using post-tensioning techniques to assemble multistory laminated veneer lumber (LVL) buildings in New Zealand (Palermo et al. 2005; Buchanan et al. 2008) and Switzerland (Wanninger and Frangi 2014). These particular solutions, named jointed ductile connections or hybrid systems, are on the basis of post-tensioning techniques to assemble structural LVL members for shear wall systems, and are designed to control rocking deformations during seismic loading. The post-tensioning connections also help structures self-center after a seismic event. These systems have been proposed and successfully tested using concepts that were originally developed for high-performance seismic-resisting precast concrete buildings, and are currently being approved in major seismic codes and design guidelines worldwide [NZS 3101 (NZS 2006); EC8 (CEN 2003); ACI 374.1-05 (ACI 2005); ACI ITG 5.2-09 (ACI 2009); and fib (fédération internationale du béton) Bulletin 27 (fib 2003)].

These studies provide the impetus for developing a new hybrid building system in which the post-tension rocking CLT panels are coupled with traditional light-frame wood constructions. This coupled system has a number of key advantages to conventional light-frame wood buildings, including: (1) improving the ability to include open floor plans; (2) having the ability to self-center after a seismic event; therefore, increase the stability and resiliency of the building; (3) having higher gravity and lateral load resistance; (4) having better response to seismic events with energy dissipation from light-weight wood systems; and thus, (5) becoming more sustainable structures.

Concept of Jointed Ductile Connections

The concept of jointed ductile connections (or hybrid systems) was first introduced in the Precast Seismic Structural Systems (PRESS) Program at the University of San Diego (Priestley 1991; Priestley et al. 1999; Priestley and Tao 1993). Under the program, several tests were conducted for precast concrete walls and frames. These systems, which are comprised of precast members connected by unbonded post-tensioning steel and bonded reinforcements, showed excellent seismic performance. A rocking motion between elements, causing a gap opening at the connection interface and inelastic deformation under the form of reinforcing steel yielding, resulted in no damage in the structural components.

The hybrid system properties include both recentering and energy dissipation. The unbonded post-tensioning provides recentering capacity, whereas energy dissipation is caused by damages of internal steel bars, external dissipation devices, or special connectors. The combination of these behaviors results in a recentering dissipation hysteresis that has a flag shape (Fig. 2). The advantage of flag-shaped hysteresis is that the residual deformation after a seismic event will be reduced significantly or eliminated, which helps to improve structural stability. In hybrid systems, inelastic deformations often are allowed at specified critical regions or connections, which are easy to repair or replace. This configuration ensures that the primary structural members remain elastic with no damage. The jointed ductile connections solution has been included in several seismic codes or design guidelines in seismic-prone countries, for example, fib Bulletin 27 (fib 2003), EC8, AIJ, ACI 374.1-05 (ACI 2005), ACI ITG 5.2-09 (ACI 2009), and NZS 3101 (NZS 2006).

Because of its useful features, the hybrid system application has been extended to other material, such as steel moment-resisting frames and multistory buildings using LVL panels (Buchanan et al. 2011). A moment-rotation prediction procedure was developed by

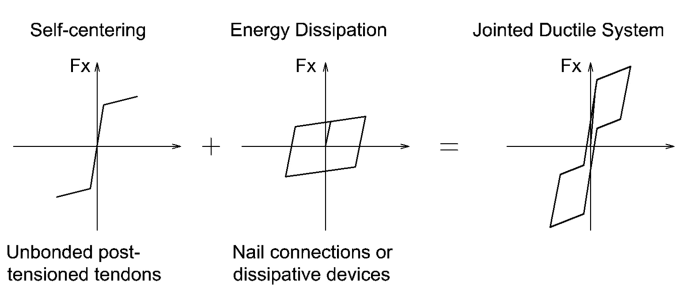

Fig. 2. Idealized flag-shaped hysteresis behavior in a hybrid connection (data from fib 2003; NZS 3101 2006)

Downloaded from ascelibrary.org by Thang Dao on 09/07/16. Copyright ASCE. For personal use only; all rights reserved.

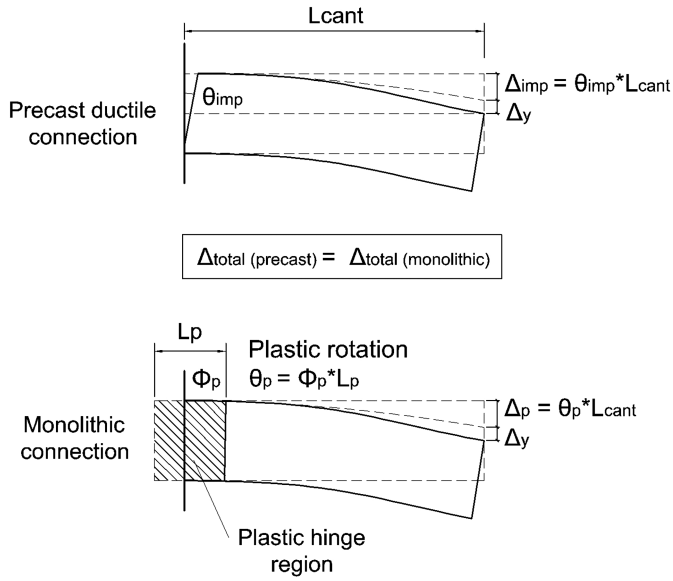

Fig. 3. Monolithic beam analogy (data from Pampanin et al. 2001)

Pampanin et al. (2001), referred to as monolithic beam analogy (MBA), and then revised to become the modified monolithic beam analogy (MMBA) (Palermo 2004), which is applicable for timber multistory seismic-resistant structures.

Numerical Model for Hybrid Systems Using CLT and LiFS Wall

MBA and MMBA

The MBA initially was introduced by Pampanin et al. (2001) for precast concrete jointed ductile connections. Pampanin et al. (2001) analyzed the difficulties in determining the strain in the prestressing steel and the position of the neutral axis when the gap opening occurs in the jointed ductile connections. Because the strain compatibility in the section level cannot be used, a global strain compatibility relationship was proposed. The equation was derived from an analogy between a precast (jointed ductile member) and an equivalent strain compatible member (monolithic member) (Fig. 3) referred to as the MBA. The MBA was implemented later into fib (2003) design guidelines and into the New Zealand Concrete Structures Standard [NZS 3101 (NZS 2006)] provisions for precast concrete jointed ductile connections.

Palermo (2004) revised the MBA, which originally focused on the plastic domain of the rotation portion of the MMBA. The preyielding behavior is included by considering the decompression and yielding points, as shown in Figs. 4(a and b). See the Appendix for more details of MBA and MMBA equations used in the derivation of this study.

Application of Jointed Ductile Connection Theory to Prestressed Timber

Overview

Because of the unique material properties of timber and its connections, alterations from the existing precast concrete design procedure were needed. Newcombe (2007) introduced the following necessary adjustments for timber material to apply MMBA:

1. The equivalent monolithic timber member will be assumed to have no tensile capacity, so that the analogy between the monolithic beam and the jointed ductile beam is ensured.
2. The timber connection remains in the elastic range when the modified MBA is applied. Thus, Eq. (27) is adequate for calculating the timber strain in the compression zone.
3. A linear stress-strain relationship is assumed for the timber in compression.
4. It is assumed that when the tendon is within the compression zone, the shortening deformation of the member is very small and can be neglected, so there is no loss in the post-tensioning force because of member compression deformation.

Assumptions in Modeling Prestressed CLT Walls

The following additional assumptions are proposed in this paper to achieve a better model of post-tensioned CLT walls:

1. When the gap opening reaches the tendon location, the tendon elongation triggers an increase in tendon force, which causes an anchorage slip. It is assumed that the magnitude of anchorage set is linearly proportional to the difference between the new tendon force and the maximum previous tendon force.
2. The friction between the tendon and the bored hole also is taken into consideration. In prestressed concrete members, there are two types of friction: wobble friction and curvature friction. In post-tensioned CLT members, the wobble friction is significant, whereas the curvature friction is neglected by

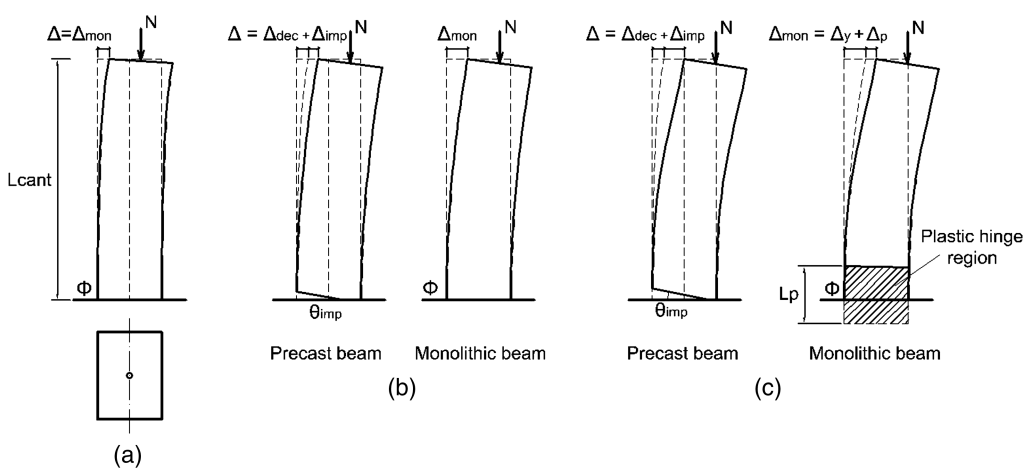

Fig. 4. Modified monolithic beam analogy: (a) $0 \le \theta \le \theta_{dec}$; (b) $\theta_{dec} \le \theta \le \theta_y$; (c) $\theta_y \le \theta \le \theta_u$ (data from Palermo 2004)

Downloaded from ascelibrary.org by Thang Dao on 09/07/16. Copyright ASCE. For personal use only; all rights reserved.

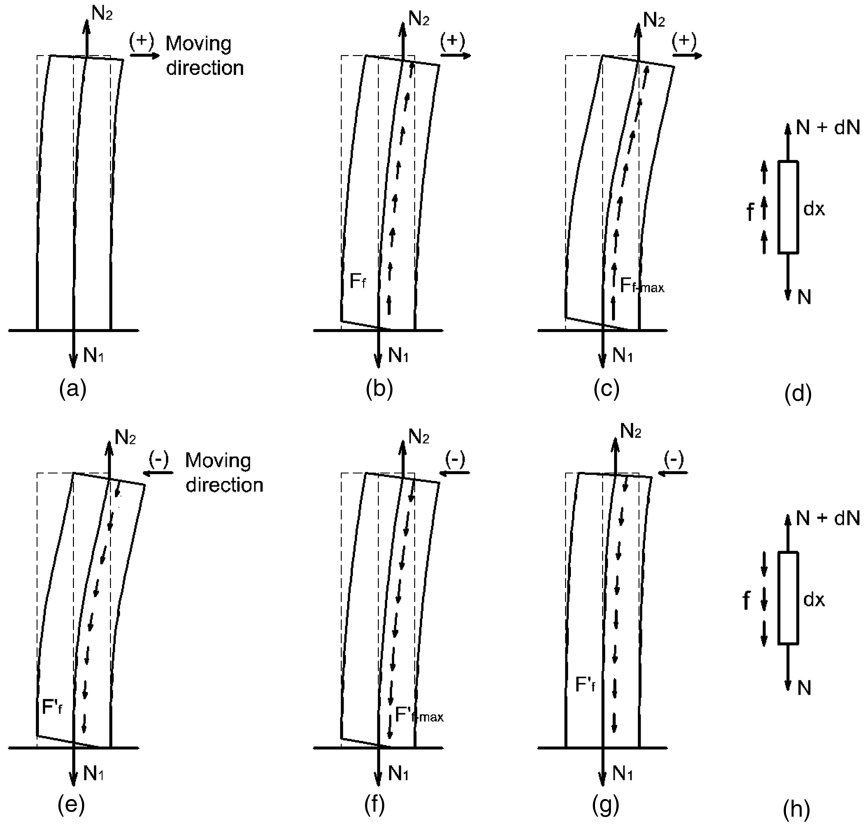

Fig. 5. Development of friction force on cable as the panel moves in the right half of the moving cycle: Stage 1: $F_f = 0$; (b) Stage 2: F_f increase from 0 to $F_{f\text{-max}}$; (c) Stage 3: $F_f = F_{f\text{-max}}$; (d) force balance of an infinitesimal cable length in positive direction; (e) Stage 4: change direction; (f) Stage 5: $F_f = F'_{f\text{-max}}$; (g) Stage 6: F_f decreases from $F'_{f\text{-max}}$ to 0; (h) force balance of an infinitesimal cable length in negative direction

default because of the assumption of neglecting member deformation.

In a half of a moving cycle, there are six stages for friction variation (Figs. 5 and 6). In the first stage [Fig. 5(a)], the CLT wall moves away from the original position (the positive direction), and the gap opening does not appear or does not reach the tendon location, so there is no friction in the tendon. As soon as the gap opening starts to result in a tendon elongation (Stage 2), the friction increases quickly from zero to its maximum magnitude [Fig. 5(b)]. In the next stage, the friction remains at its maximum value until the wall movement direction begins to change [Fig. 5(c)]. Although the member changes direction (Stage 4), i.e., moving to the original position (negative direction), the friction force also changes its direction and magnitude (from $F_{f\text{-max}}$ to $F'_{f\text{-max}}$) [Fig. 5(e)]. Then, in Stage 5, the friction maintains its maximum value until the gap opening at the tendon location closes as the panel moves to the original position [Fig. 5(f)]. At the original position, the friction force value returns to zero [Fig. 5(g)] and then bounces back to the maximum (and the force direction changes) as the panel keeps moving to the left (the moving direction now changes from negative to positive). A similar friction force protocol occurs on the left side because of the symmetrical properties of the panel.

In Fig. 5, N_2 denotes the tensile force acting at the top end of the tendon, N_1 is the tensile force in the tendon acting at the bottom end, and F_f and F'_f are friction forces between the tendon and the bored hole when the panel moves away and back to the center position, respectively.

The experimental parameter K_l (Fig. 6) indicates the difference in panel displacement when the friction force changes its direction and bounces back to the maximum.

3. To convert from the real stress distribution in the compression zone on the connection interface to the triangular stress distribution, a correction factor λ_c for the depth of neutral axis was introduced and obtained by fitting the numerical model result to the experimental data.

Effect of Friction

First, consider the wall moving away from the original position at which the friction direction acting on the tendon is upward;

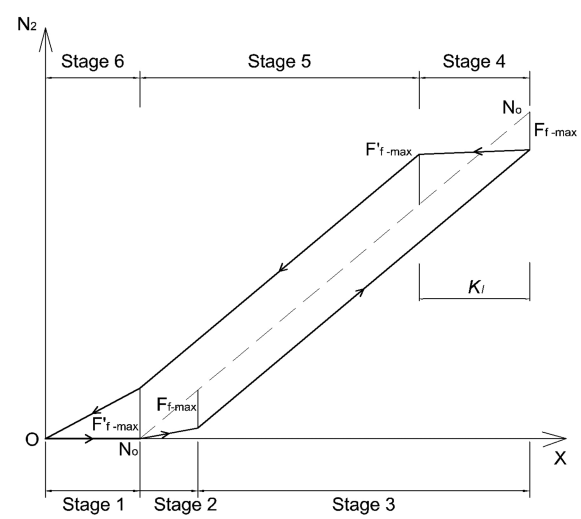

Fig. 6. Development of the tendon force acting at the top end (N_2) when the panel moves in the right half of the rocking cycle

Downloaded from ascelibrary.org by Thang Dao on 09/07/16. Copyright ASCE. For personal use only; all rights reserved.

therefore, the equilibrium equation for the tendon can be expressed as

$$N_2 + F_{f-\max} - N_1 = 0 \tag{1}$$

Now, consider an infinitesimal length dx for the tendon, and write the equilibrium equation for it [Fig. 5(d)]

$$N + dN + f dx - N = 0 \qquad \therefore\ dN = -f dx \tag{2a}$$

in which

$$f = N \times K_f \tag{2b}$$

where f = friction force per length unit; N = internal force at the location x; and K_f = wobble friction coefficient.

From Eqs. (2a) and (2b)

$$\frac{dN}{N} = -K_f dx$$

Integrating both sides and solving for N

$$N = N_1 e^{-K_f x} \tag{2c}$$

For $x = L_{ub}$

$$N_2 = N_1 e^{-K_f L_{ub}} = \mu N_1 \tag{3}$$

in which

$$\mu = e^{-K_f L_{ub}} \tag{4}$$

From Eqs. (1) and (3)

$$F_{f-\max} = (1-\mu) N_1 \tag{5}$$

The total tendon elongation

$$\Delta = \Delta_0 + \Delta_t = \int_0^{L_{ub}} \varepsilon dx = \int_0^{L_{ub}} \frac{N}{E_{ps} A_{ps}} dx \tag{6}$$

where Δ_0 = initial elongation in the tendon because of prestressing; and Δ_t = additional tendon elongation.

Substituting Eq. (2c) into Eq. (6):

$$\Delta = \Delta_0 + \Delta_t = \int_0^{L_{ub}} \frac{N_1 e^{-K_f x}}{E_{ps} A_{ps}} dx$$
$$= \frac{N_1}{-K_f E_{ps} A_{ps}} \int_0^{L_{ub}} e^{-K_f x} d(-K_f x) = \frac{(1-\mu) N_1}{K_f E_{ps} A_{ps}}$$
$$\therefore\ N_1 = \frac{K_f L_{ub}}{(1-\mu)} \left(N_0 + \Delta_t \frac{E_{ps} A_{ps}}{L_{ub}} \right) \tag{7}$$

where N_0 = tendon load corresponding to the elongation Δ_0.

When the wall moves back to the original position, Eqs. (1), (2a), (2c), (3), (5), and (7) become the following, respectively:

$$N_2 - F'_{f-\max} - N_1 = 0 \tag{8}$$

$$dN = df \tag{9a}$$

$$N = N_1 e^{K_f x} \tag{9b}$$

$$N_2 = N_1 e^{K_f L_{ub}} = \frac{N_1}{\mu} \tag{10}$$

$$F'_{f-\max} = \frac{(1-\mu) N_1}{\mu} \tag{11}$$

$$N_1 = \frac{\mu K_f L_{ub}}{(1-\mu)} \left(N_0 + \Delta_t \frac{E_{ps} A_{ps}}{L_{ub}} \right) \tag{12}$$

In Stages 2, 4, and 6, the change in friction force is assumed to be linear with the change in displacement.

Hysteresis Model for Light-Frame Wood Shear Walls

The hysteresis behavior of LiFS has been represented by a numerical model, namely the Consortium of Universities for Research in Earthquake Engineering (CUREE) 10-parameter model (Fig. 7), developed by Folz and Filiatrault (2001) and a number of researchers (Folz and Filiatrault 2004; 2007; Pang and Rosowsky 2010; Pang et al. 2010; Pei and van de Lindt 2011b).

This hysteresis model of sheathing-to-frame connectors was developed on the basis of a number of path-following rules that can reproduce the response of the connector under general cyclic loading. The envelope curve, which was proposed originally by Foschi (1977), is described by the following nonlinear load-deformation relationship:

$$F = \mathrm{sgn}(\delta).(F_0 + r_1 K_0 |\delta|).[1 - \exp(-K_0 |\delta| / F_0)] \quad \text{for } |\delta| \le |\delta_u| \tag{13a}$$

$$F = \mathrm{sgn}(\delta).F_u + r_2 K_0.[\delta - \mathrm{sgn}(\delta).\delta_u] \quad \text{for } |\delta_u| < |\delta| \le |\delta_F| \tag{13b}$$

$$F = 0 | \text{for } \delta| > |\delta_F| \tag{13c}$$

in which F_0 = intercept of strength for the asymptotic line to the envelope curve; δ_u = displacement at the peak load ($\delta_u > 0$); δ_F = failure displacement; K_0 = initial stiffness of the hysteretic curve ($K_0 > 0$); r_1 = stiffness ratio of the asymptotic line to the envelope curve ($0 < r_1 < 1.0$); and r_2 = stiffness ratio of the descending segment of the envelope curve ($r_2 < 0$). The stiffness ratio of the unloading segment off the hysteretic backbone curve is represented by r_3 ($r_3 < 1$), whereas r_4 stands for the stiffness ratio of the pinching part of the hysteretic curve ($r_4 > 0$). F_1 is the zero-displacement intercept strength for the pinching part. The reloading path after the pinching part is described by the degrading stiffness K_p, which is a function of the previous loading history

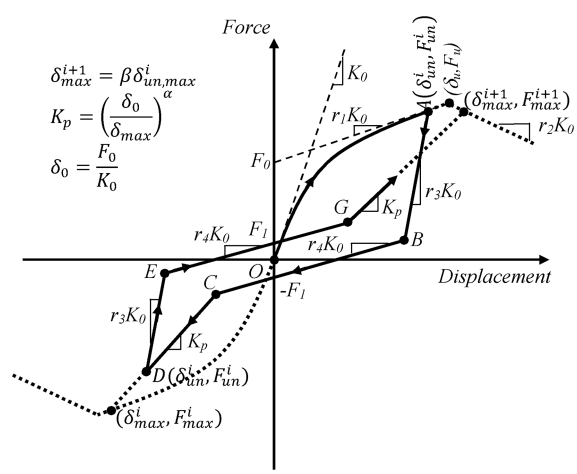

Fig. 7. Ten-parameter hysteresis model (data from Folz and Filiatrault 2001, © ASCE)

Downloaded from ascelibrary.org by Thang Dao on 09/07/16. Copyright ASCE. For personal use only; all rights reserved.

$$K_P = K_0\left(\frac{\delta_0}{\delta_{\max}}\right)^{\alpha} \tag{14}$$

in which $\delta_0 = F_0/K_0$; $\delta_{\max} = \beta\delta_{un}$; δ_{un} = maximum unloading displacement off the envelope curve; and α and β = hysteretic model parameters involving the stiffness degradation and energy degradation ($\alpha > 0$ and $\beta > 0$).

Applying the CUREE 10-parameter model for connectors between the shear walls and the CLT wall provides the nail forces (F_i^{up} and F_j^{down}) subjected to both sides of the CLT wall. When the CLT wall moves in the right half of the rocking cycle, the direction of nail forces on the right edge of the wall is upward, whereas that on the left edge is downward, and vice versa.

Calculation Procedure

Under the imposed lateral displacement at the top of the wall, the CLT wall shows both rocking and self-centering behaviors. The neutral axis and imposed rotation of the rocking interface section and the tendon load are unknown. However, they can be determined on the basis of the MMBA theory and equilibrium equations, with the following steps:

1. Choose an initial depth for the compressive zone (c) (Fig. 8).
2. Calculate the decompression curvature (ϕ_{dec}), total curvature (ϕ), and the interface gap rotation (θ_{imp}) using Eqs. (22), (24), and (26), respectively. On the basis of θ_{imp}, the elongation strain in the tendons (ε_T), displacement of connections (nails) in the uplifted edge, and the other edge of the wall, (Δ_i^{up} and Δ_j^{down}, respectively, if available) can then be computed

$$\varepsilon_T = \frac{\theta_{\text{imp}} \times (x_T - c)}{L_{ub}} \tag{15a}$$

$$\Delta_i^{\text{up}} = -\Delta_l - \frac{\Delta \times \Delta_g}{H} \tag{15b}$$

$$\Delta_j^{\text{down}} = \frac{\Delta \times \Delta_g}{H} \tag{15c}$$

$$\Delta_l = \theta_{\text{imp}} \times (L_w - c) \tag{15d}$$

where x_T = coordinate of tendon counting from the rocking point; L_{ub} = unbonded length of the tendon; Δ = imposed lateral displacement at the top; Δ_g = gap between the vertical edges of the CLT wall and that of the connected shear wall; Δ_l = gap opening at the bottom of the CLT wall; and H and L_w = height and width of the CLT wall, respectively.

The effect of anchorage slip also is taken into account as

$$\varepsilon_{ld} = \frac{P_T - P_{T\text{dec}}}{K_{ld}} \tag{15e}$$

where P_T = tendon load; $P_{T\text{dec}}$ = maximum tendon load before the decompression point; and K_{ld} = anchorage set coefficient determined by the test data of tendon load dropping at the wall's original position.

Then, the total tendon strain (ε_{ps}) and forces because of nails on the basis of hysteresis loop (F_i^{up} and F_j^{down}) can be computed

$$\varepsilon_{ps} = \varepsilon_{To} + \varepsilon_T - \varepsilon_{ld} \tag{15f}$$

where ε_{To} = initial tendon strain.

The tendon load P_T is equal to the tensile force acting on the top end of tendon N_2. From Eqs. (1) and (8), the following relationship is obtained:

$$N_1 = P_T \pm F_f \tag{16}$$

N_1 can be calculated by Eq. (7) or Eq. (12) depending on whether the wall is moving away or moving to the original position. F_f is the friction force between the tendon and the bored hole.

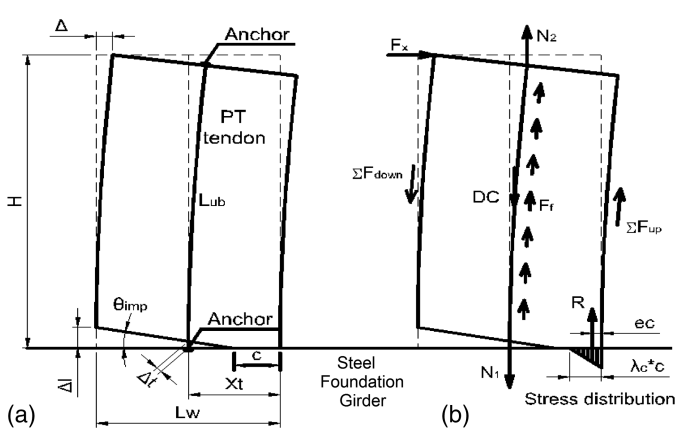

Fig. 8. Friction force in post-tensioned tendon: (a) dimensions used in the text; (b) forces acting on tendon and CLT panels

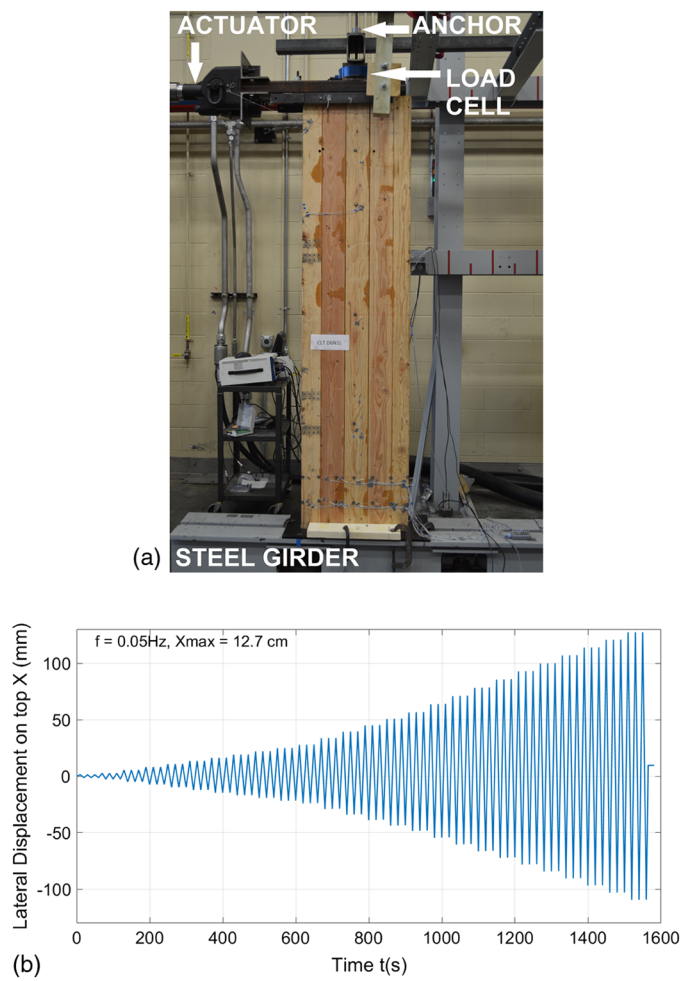

Fig. 9. Test setup and test protocol for single CLT panel: (a) experimental setup; (b) cyclic test protocol for post-tensioned CLT wall testing

Downloaded from ascelibrary.org by Thang Dao on 09/07/16. Copyright ASCE. For personal use only; all rights reserved.

3. On the basis of the equilibrium equation, the reaction force from the foundation (R) can then be determined

$$\sum F_y = DC + P_T \pm F_f + \sum_{j=1}^{m} F_j^{\text{down}} - \sum_{i=1}^{n} F_i^{\text{up}} - R = 0$$

$$\therefore\ R = DC + N_1 + \sum_{j=1}^{m} F_j^{\text{down}} - \sum_{i=1}^{n} F_i^{\text{up}} \tag{17}$$

where DC = dead load of the wall.

4. Update c.

From the assumption of the stress distribution in the compression zone of the connection interface

$$R = \frac{1}{2}(\lambda_c c) \times b \times \lambda_c = \frac{1}{2}(\lambda_c c) \times b \times \varepsilon_c \times E_{\text{con}}$$

$$\therefore\ c = \sqrt{\frac{2R}{\lambda_c b \phi E_{\text{con}}}} \tag{18}$$

where b = thickness of the CLT wall; E_{con} = modulus of elasticity of timber at the connection interface; and λ_c = correction factor for the depth of neutral axis ($\lambda_c < 1$). Both E_{con} and λ_c are obtained by fitting the model results to the experiment data.

5. Iterate Steps 2–4 until c converges.
6. Calculate F_x on the basis of the moment equilibrium equation

$$F_x = \sum_{i=1}^{n} \frac{e_c}{H} F_i^{\text{up}} + \sum_{j=1}^{m} \frac{(L_w - e_c)}{H} F_j^{\text{down}} + (DC + N_1)\frac{(L_w/2 - e_c)}{H} \tag{19}$$

where e_c = distance from the location of reaction R to the unlifted edge of the wall.

Experimental Validation

Single Post-Tensioned CLT Wall Test

Test Protocol

The CLT wall used in the test is a 13.34 cm (5.25 in.) thick, 0.61 m by 2.44 m (2 ft by 8 ft) panel. The CLT panel was tied to a steel foundation beam using one 15.24 mm (0.6 in.) diameter prestressing tendon (Grade 270) through the center-bored hole in the CLT panel. The unbonded tendon was anchored using a monostrand anchor at the bottom; meanwhile, a load cell was installed into the other end, which was anchored to the top of the CLT wall. The tendon was post-tensioned to a stress of 929,343 kPa (134,79 ksi) [$0.555 f_{py}$, in which $f_{py} = 0.9 f_{pu} = 1{,}675{,}426$ kPa (243 ksi) is the yield stress of the post-tensioned (PT) strand] resulting in an initial clamping load of 130.11 kN (29.25 kips). A cyclic test was conducted with a frequency of 0.05 Hz and a maximum displacement of 12.7 cm (5.017 in.) (approximately 5.23% drift) following the displacement protocol as shown in Fig. 9.

Test Results and Numerical Validation

When the gap opening propagated to the tendon position, the depth of the neutral axis was smaller than the depth of tendon in the rocking interface section. When the lateral displacement reached a new maximum unloaded value, the test revealed that the maximum tendon force increased, but the force in tendon at the original wall position decreased [Fig. 10(a)]. This is possibly because of the anchorage slip phenomenon, which occurs and then causes prestressing losses. Moreover, because of the small bored hole, contact between the tendon and the hole led to a considerable friction effect, which was a source of pinching in the hysteresis behavior of the wall. The friction force is also a major cause of the observed difference in leading and trailing tendon load in each

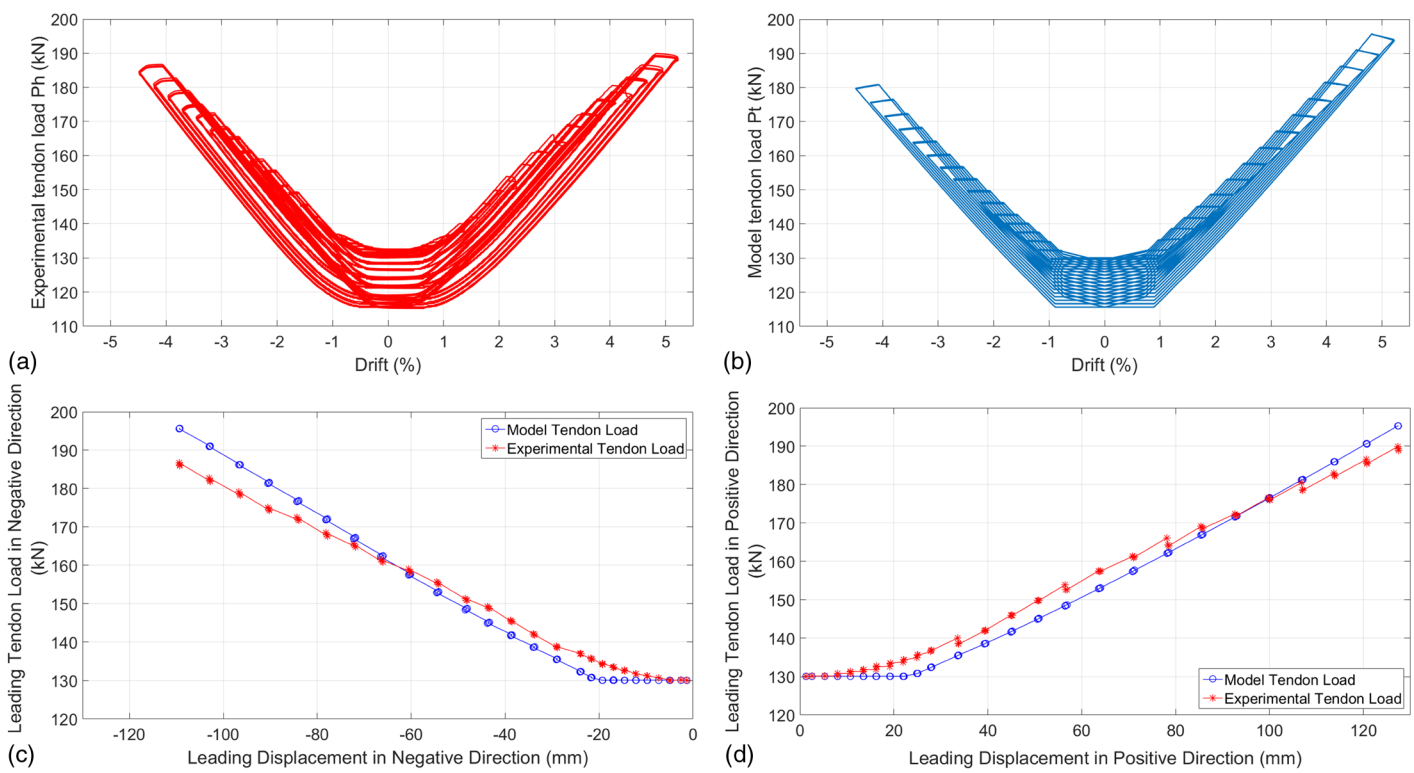

Fig. 10. Force in tendon under lateral cyclic loading: (a) tendon load-drift relationship from experiment results; (b) tendon load-drift from numerical model; (c and d) leading tendon loads corresponding to maximum displacements in each cycle in both negative and positive directions

Downloaded from ascelibrary.org by Thang Dao on 09/07/16. Copyright ASCE. For personal use only; all rights reserved.

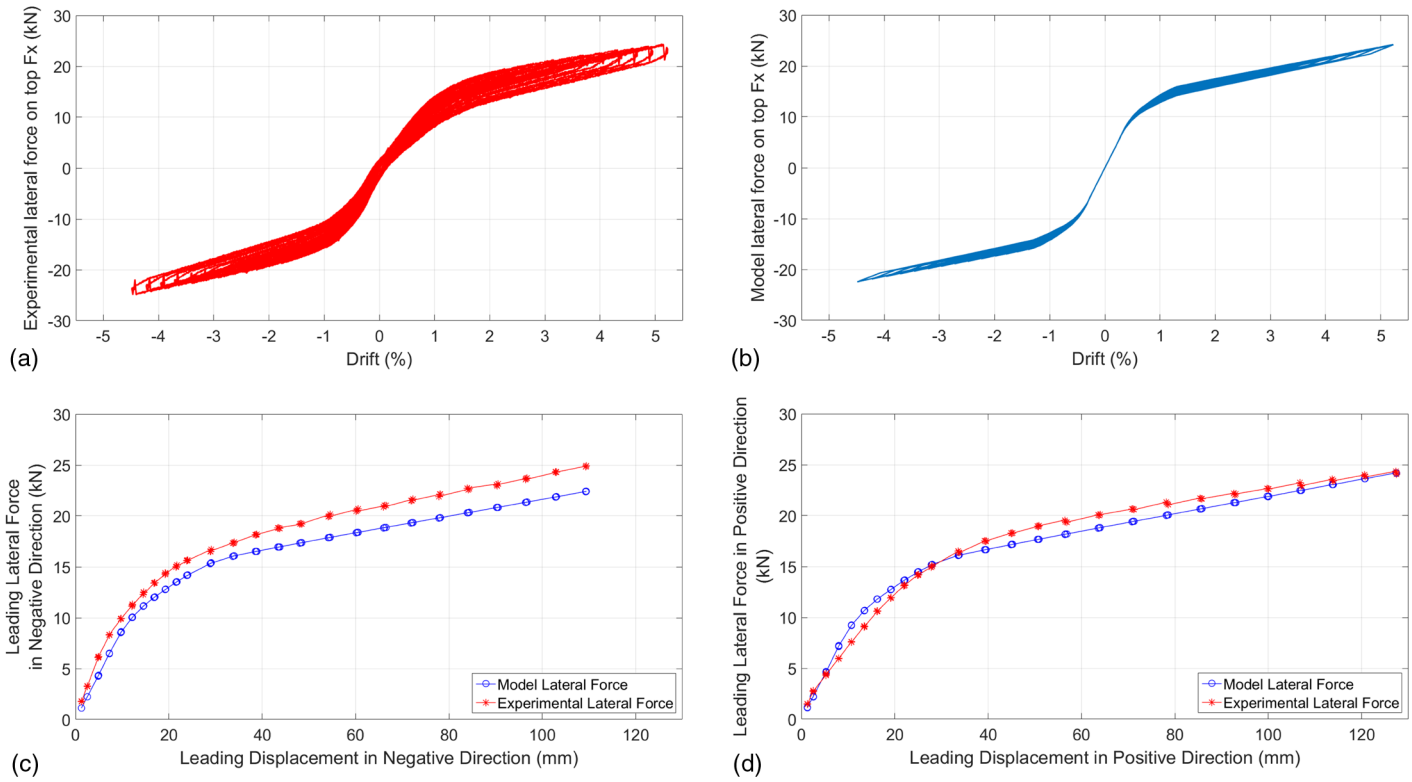

Fig. 11. Hysteresis behavior of CLT panel: (a) experimental data and (b) model result; and leading lateral forces corresponding to maximum displacements in each cycle in (c) negative direction; (d) positive direction

half rocking cycle [Fig. 10(a)], as presented in the section of "Assumptions in Modelling Prestressed CLT Walls." No considerable damage to the CLT wall was observed after testing.

The value of experimental parameters E_{con} changed from (1,723,686 kPa) (250 ksi) for Case 1 (pre-decompression point) to (6,894,745 kPa) 1,000 ksi for Case 2 (between decompression and yielding). Values of other experimental parameters: $\lambda_c = 1.5$, $K_f = 15.75 \times 10^{-3}$ m^{-1}, $K_{ld} = 124{,}550.2$ kN-m/m, and $K_l = 0.0102$ m were obtained by fitting the model curves to the experiment data. Fig. 10(a) shows the tendon load obtained from load cell data. With the assumptions of losses because of the anchorage slip and friction effect, the behavior of the tendon can be modeled accurately as shown in Fig. 10(b). Figs. 10(c and d) illustrate the leading tendon loads corresponding to maximum displacements in each cycle in both negative and positive directions. Overall, the error of the tendon load in the numerical model was under 5%.

However, the energy dissipation sources of the CLT panel were modeled merely on the basis of the tendon losses and friction force because the behavior of panel and connection interface was assumed in the elastic range. As a result, the idealized lateral force acting on the top of the panel did not fit well with the experimental data. The hysteresis behavior and energy dissipation can be observed in Fig. 11(a), but the energy dissipation is not clearly shown in Fig. 11(b). Some damages in the contact surface caused inelastic behavior of the CLT material, which did not meet with the assumptions made in the "Overview" section. However, this was acceptable because of the energy dissipated by this damage was small compared with that of light-frame wood system. For better accuracy, this problem should be taken into account in future research. Generally, the trend of lateral forces obtained by the numerical model reasonably reflected the change in the experimental forces. Figs. 11(c and d) present the lateral force on the top of the

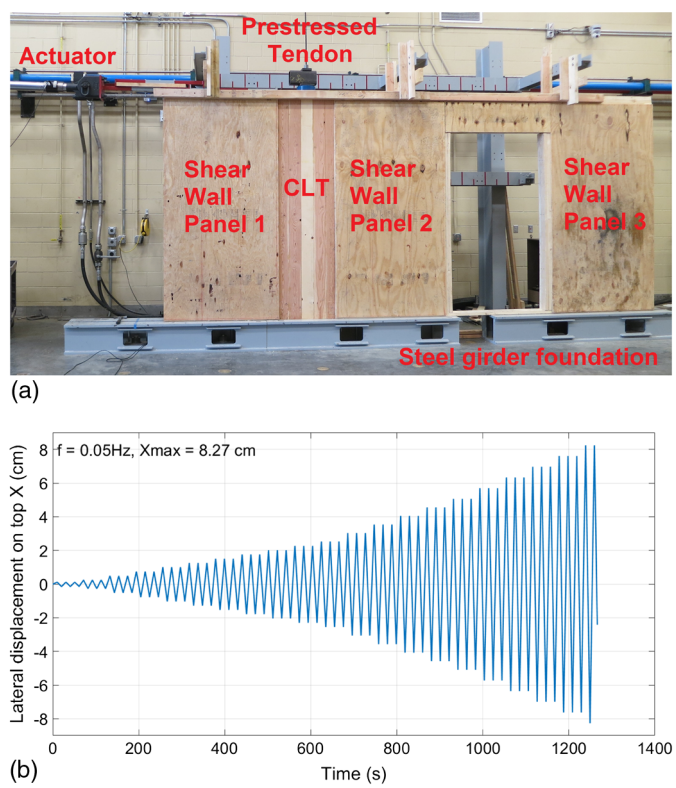

Fig. 12. Test setup and test protocol for hybrid wall experiment: (a) experimental setup; (b) cyclic test protocol for hybrid wall

Downloaded from ascelibrary.org by Thang Dao on 09/07/16. Copyright ASCE. For personal use only; all rights reserved.

wall. The leading force corresponding to the maximum displacement in the positive direction was predicted well with only a maximum difference of 1.646 kN (0.37 kips), whereas in the negative direction it was underestimated by 2.491 kN (0.56 kips).

Hybrid Wall Test

Cyclic Testing Arrangement

The same CLT panel configuration as in the single prestressed CLT wall test was integrated into a typical LiFS line consisting of three panels, 2.44 m (96 in.) in height and 1.22 m (48 in.) wide, a 0.61 m (2 ft) opening (replaced by CLT panel) and a 1.22 m (4 ft) opening (Fig. 12). Six 16-penny 89 mm ($3-1/2$ in.) hot dipped galvanized common nails were used to connect the CLT panel and the shear wall at each edge. At the bottom of each panel, there were three hold-down bolts [$d = 15.88$ mm ($5/8$ in.)] connected to the steel beam foundation. The traditional wood shear wall had a similar configuration to the full-scale shear wall tested in the study of Shao et al. (2014), with only a difference in dimensions of the openings. In the hybrid wall test, a 15.24 mm (0.6 in.) diameter prestressing tendon (Grade 270) also was used and post-tensioned to an initial clamping load of 100.97 kN (22.70 kips). A cyclic test was conducted with a frequency of 0.05 Hz and a maximum displacement of 8.27 cm (3.25 in.) (approximately 3.39% drift) following the displacement protocol as shown in Fig. 12.

Test Results and Numerical Model Validation

The behavior of the hybrid wall was a combination of the shear wall and the CLT panel. Whereas five experimental parameters [Fig. 13(b)] for the CLT panel were kept the same as those in the single prestressed CLT wall test, the 10 parameters for the LiFS model were obtained from the study by Shao et al. (2014). Because there were only six nails arranged on each edge of the CLT panel, the effect of nail connections on the behavior of the panel was small and, therefore, can be neglected. Numerical results from

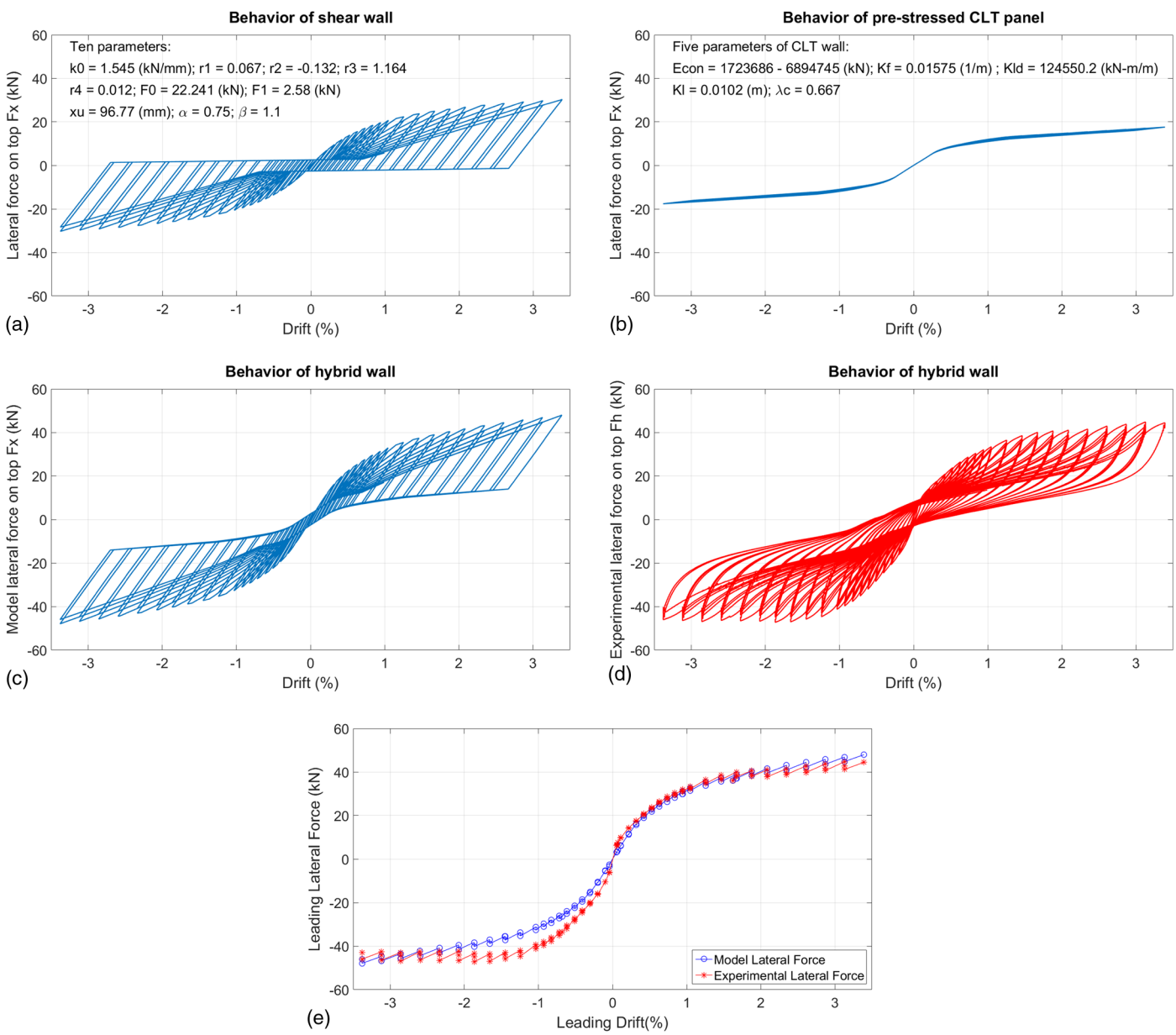

Fig. 13. Hysteresis behavior of hybrid wall: (a) shear wall; (b) prestressed CLT panel; (c) hybrid wall; (d) experimental data of lateral force–drift (%) relationship for hybrid wall; (e) leading lateral force–leading drift: comparison of model result and experimental data

Downloaded from ascelibrary.org by Thang Dao on 09/07/16. Copyright ASCE. For personal use only; all rights reserved.

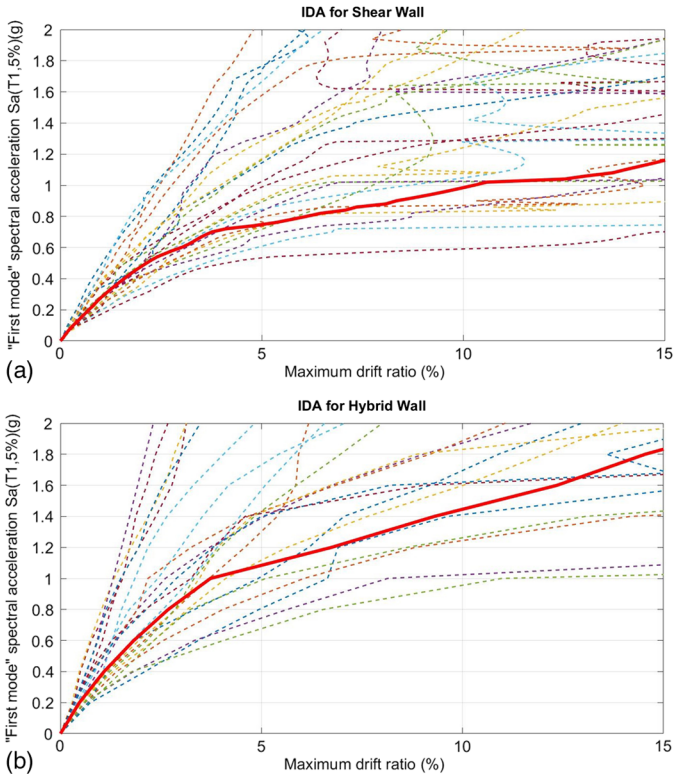

Fig. 14. Incremental dynamic analysis results for maximum wall drift: (a) shear wall result; (b) hybrid wall result

the analysis for traditional wood shear wall and prestressed CLT panel are shown in Figs. 13(a and b), respectively. The numerical behavior of the hybrid wall is shown in Fig. 13(c) and compared with the experimental data in Fig. 13(d). Fig. 13(e) shows a comparison of the numerical and experimental force-drift envelope. Fig. 13 shows that the numerical model provides a reasonable prediction of hysteretic behavior for the hybrid wall. Because of the asymmetry of the experimental data, the numerical model fitted well for the lateral force in positive displacement (first quadrant); however, there was a discrepancy in the force in the negative displacement (third quadrant).

Incremental Dynamic Analysis

The incremental dynamic analysis (IDA) procedure, a comprehensive review that was presented by Vamvatsikos and Cornell (2002), has become a powerful tool for investigating the performance of structures subjected to earthquake ground motions. Both the hybrid wall and a shear wall with the same configuration used in the hybrid wall were analyzed on the basis of a suite of 22 ground-motion pairs [PEER NGA (PEER 2008)] in increasing seismic intensity levels. The hybrid wall and traditional wood shear wall each carried a total load of 136.027 kN (30.58 kip) and 148.384 kN (33.358 kip), respectively. These loads included their self-weight, dead load, and effective live load from their distributed floor areas. The initial stiffness of the hybrid wall and the traditional wood shear wall were 2.260 kN/m (20 kip/in.) and 0.997 kN/m (8.82 kip/in.), respectively. Both walls were assumed to have a damping ratio of 5%.

The collapse limit of 7% was used in this study for the traditional shear wall as recommended by the study by Pei et al. (2013). This drift limit also has been used in many projects before (e.g., Christovasilis et al. 2009; Pang et al. 2010; ATC 2009; van de Lindt et al. 2011). As a result, the traditional wood shear wall was considered to fail if the lateral displacement exceeded 17.07 cm (6.72 in.), and only the CLT panel in the hybrid wall was numerically present after that drift level. It was expected that the collapse limit for hybrid walls would be higher than 7%; however, this prediction needs a validation from future experimental studies. In this study, the collapse limit for LiFS in the hybrid system was taken as 7% for consistency with other studies, and the CLT remained elastic afterward.

Figs. 14(a and b) illustrate the maximum drift IDA results for the traditional wood shear wall and hybrid wall, respectively. The bold line in each figure represents the mean IDA curve. Obviously, the mean IDA curves of the two walls in the drift range of 10% show a similar pattern, with a softening behavior at approximately 3.7% drift. However, the initial slope of the mean curve for the hybrid wall was steeper. The mean value of the spectral acceleration for the traditional wood shear wall at the collapse drift limit was 0.84 g, whereas that of the hybrid wall was 1.2 g. This observation is reasonable because the hybrid wall had a higher stiffness and a better self-centering capacity than that of the LiFS. Fig. 14 also shows that the mean IDA curve for the hybrid wall continued to increase, whereas the mean IDA curve for the traditional wood shear wall flattened out after reaching the collapse drift. This is because the CLT wall was modeled to work elastically, and only the elastoplastic behavior of the high-strength steel tendon was taken into consideration on the basis of PCI (2010). Further studies on the inelastic behavior of CLT walls should be investigated to obtain a more comprehensive picture of a hybrid walls' seismic response.

Summary and Conclusions

The numerical model of a post-tensioned CLT wall was developed on the basis of the MMBA and on assumptions about the friction between the tendon and the bored hole, and the anchorage slip. This model integrated with the well-known CUREE 10-parameter model for shear walls, resulting in acceptable accuracy compared with the experimental data. The losses in tendon stress, the development of the tendon load, and the hysteresis behavior of the hybrid wall were modeled and consistent with experimental data. However, there is still room for improvement. The modeled hysteresis behavior of the CLT walls was not highly accurate in terms of energy dissipation. It might be because of an imperfection in the tested CLT panels or an inelastic deformation at the bottom of panels, although the panels were modeled in the elastic range. Moreover, the behavior of the panel with large lateral displacements (for example, in the incremental dynamic analysis) needs more research. Although the inelastic behavior of tendon steel was considered in the model, the panel was still assumed elastic. That is not an accurate assumption if the tendon stress reaches over its elastic limit, and/or the panel contact surface is crushed under high compression forces. Further study for the behavior of hybrid systems beyond these limits is recommended.

Appendix. Fundamental Equations of MBA and MMBA Methods

MBA for Precast Concrete

The MBA (Pampanin et al. 2001) assumes that the total displacement in the monolithic cantilever consists of elastic deformation and plastic rotation about the centroid of the plastic hinge. Conversely, the displacement of the precast beam is the sum of the elastic deformation and an opening of a gap at the rocking interface, which is because of an imposed rigid rotation approximately a

Downloaded from ascelibrary.org by Thang Dao on 09/07/16. Copyright ASCE. For personal use only; all rights reserved.

zero-length plastic hinge, at the joint interface similar to the monolithic beam.

For the same total imposed displacement, the elastic deformations are the same in the two beams with identical geometry and reinforcement

$$\theta_{\text{imp}} L_{\text{cant}} = (\phi - \phi_y) L_p (L_{\text{cant}} - 0.5 L_p) \tag{20}$$

The relationship between concrete strain and neutral axis position is derived from the equal plastic deformations in the two beams

$$\varepsilon_c = \phi c = \left[\frac{\theta_{\text{imp}} \times L_{\text{cant}}}{(L_{\text{cant}} - \frac{L_p}{2}) L_p} + \phi_y \right] c \tag{21}$$

where ε_c = hypothetical concrete strain within the precast post-tensioned system; ϕ = curvature at connection interface of the monolithic beam; c = depth of the neutral axis at the rocking interface; θ_{imp} = imposed rotation at the rocking interface; L_{cant} = cantilever length of the element; L_p = plastic hinge length of the monolithic element; and ϕ_y = curvature at connection interface of the beam at the yielding point.

MMBA for Precast Concrete

Three ranges of deformation are illustrated in Fig. 4 and summarized in the following for brevity; refer to Palermo (2004) for more details.

1. $0 \le \theta \le \theta_{\text{dec}}$ (predecompression point):

   Before the decompression point, there is no joint rotation ($\theta_{\text{imp}} = 0$), so the gap opening does not occur at this range. Strain capability is considered valid for the jointed member and, hence, the strain within the section can be evaluated from section equilibrium directly. The displacements of two beams are the same

$$\Delta = \Delta_{\text{mon}} = \phi \frac{L_{\text{cant}}^2}{3} \tag{22}$$

2. $\theta_{\text{dec}} \le \theta \le \theta_y$ (between decompression and yielding)

   The behavior of the monolithic beam is still in the elastic region, whereas the effect of imposed rotation starts to contribute to the deformation of the jointed beam

$$\Delta = \theta_{\text{imp}} L_{\text{cant}} + \phi_{\text{dec}} \frac{L_{\text{cant}}^2}{3} \tag{23}$$

   in which ϕ_{dec} = curvature at connection interface of the beam at the decompression point

$$\phi_{\text{dec}} = \frac{2P}{b L_w^2 E} \tag{24}$$

   where P = total compression load; b and L_w = dimensions of the beam; and E = elastic modulus of the connection.

   Eqs. (22) and (24) can be derived from the behavior of a column with horizontal force and axial force acting on the top, by applying Euler beam theory.

   From the analogy between the monolithic and precast members

$$\Delta_{\text{mon}} = \Delta \tag{25}$$

   Substituting the expressions from Eqs. (22) and (23) into Eq. (25)

$$\phi \frac{L_{\text{cant}}^2}{3} = \theta_{\text{imp}} L_{\text{cant}} + \phi_{\text{dec}} \frac{L_{\text{cant}}^2}{3} \qquad \therefore \ \phi = 3 \frac{\theta_{\text{imp}}}{L_{\text{cant}}} + \phi_{\text{dec}} \tag{26}$$

   From Eq. (26)

$$\varepsilon_c = \phi c = \left(3 \frac{\theta_{\text{imp}}}{L_{\text{cant}}} + \phi_{\text{dec}} \right) c \tag{27}$$

3. For $\theta_y \le \theta \le \theta_u$ (between yielding and ultimate)

   The monolithic beam reaches the elastic limit and plastic deformation begins

$$\Delta_{\text{mon}} = \Delta_y + \Delta_p = \phi_y \frac{L_{\text{cant}}^2}{3} + (\phi - \phi_y) L_p \left(L_{\text{cant}} - \frac{L_p}{2} \right) \tag{28}$$

   Using the same relationship in Eq. (25)

$$\Delta_{\text{mon}} = \Delta \tag{29}$$

   Substituting Eqs. (23) and (28) into Eq. (29)

$$\phi_y \frac{L_{\text{cant}}^2}{3} + (\phi - \phi_y) L_p \left(L_{\text{cant}} - \frac{L_p}{2} \right) = \theta_{\text{imp}} L_{\text{cant}} + \phi_{\text{dec}} \frac{L_{\text{cant}}^2}{3}$$

$$\therefore \ \phi = \left[\frac{\theta_{\text{imp}} L_{\text{cant}} - \frac{(\phi_y - \phi_{\text{dec}}) L_{\text{cant}}^2}{3}}{L_p (L_{\text{cant}} - \frac{L_p}{2})} \right] + \phi_y \tag{30}$$

   The term $[(\phi_y - \phi_{\text{dec}}) L_{\text{cant}}^2]/3$ in the Eq. (30) illustrates the additional inclusion of the decompression curvature in the MMBA, when compared with the original MBA.

   The section strain in this range can be computed by the following equation:

$$\varepsilon_c = \left[\frac{\frac{3\theta_{\text{imp}}}{L_{\text{cant}}} - (\phi_y - \phi_{\text{dec}})}{\frac{3L_p}{L_{\text{cant}}} (1 - \frac{L_p}{2L_{\text{cant}}})} + \phi_y \right] c \tag{31}$$

Acknowledgments

The National Science Foundation provided support for this study through Grant No. CMMI-1537788. The CLT panels used in this study were provided by Forest Products Laboratory, U.S. Department of Agriculture, and that support is gratefully acknowledged. Thanks also are extended to undergraduate students at the University of Alabama who helped in building the test specimens.

References

ACI (American Concrete Institute). (2005). "Acceptance criteria for moment frames based on structural testing and commentary." *ACI 374.1-05*, Farmington Hills, MI.

ACI (American Concrete Institute). (2009). "Requirements for design of a special unbonded post-tensioned precast shear wall satisfying ACI ITG-5.1 & commentary." *ACI ITG-5.2-09*, Farmington Hills, MI.

ANSI/APA (American National Standards Institution/American Plywood Association) CLT (Cross-Laminated Timber) Standard Committee. (2012). "American national standard—Standard for performance rated cross-laminated timber." *ANSI/APA PRG 320-2012*, APA–Engineered Wood Association, Tacoma, WA.

ATC (Applied Technology Council). (2009). "Quantification of building seismic performance factors." *Project 63, FEMA P695*, Federal Emergency Management Agency (FEMA), U.S. Dept. of Homeland Security (DHS), Washington, DC.

Downloaded from ascelibrary.org by Thang Dao on 09/07/16. Copyright ASCE. For personal use only; all rights reserved.

AWC (American Wood Council's). (2015). "National design specification (NDS) for wood construction." *ANSI/AWC NDS-2015*, Leesburg, VA.

Buchanan, A. H., Bull, D., Dhakal, R., MacRae, G., Palermo, A., and Pampanin, S. (2011). "Base isolation and damage-resistant technologies for improved seismic performance of buildings." *Research Rep. No. 2011-02*, Univ. of Canterbury, Christchurch, New Zealand.

Buchanan, A. H., Deam, B., Fragiacomo, M., Pampanin, S., and Palermo, A. (2008). "Multi-storey prestressed timber buildings in New Zealand." *Struct. Eng. Int.*, 18(2), 166–173.

CEN (European Committee for Standardizations). (2003). "Design of structures for earthquake resistance." *EuroCode 8, EC8*, Bruxelles, Belgium.

Christovasilis, I. P., Filiatrault, A., Constantinou, M. C., and Wanitkorkul, A. (2009). "Incremental dynamic analysis of woodframe buildings." *Earthquake Eng. Struct. Dyn.*, 38(4), 477–496.

fib (fédération internationale du béton). (2003). "Seismic design of precast concrete building structures." *fib Bulletin 27*, International Federation for Structural Concrete, Lausanne, Switzerland.

Folz, B., and Filiatrault, A. (2001). "Cyclic analysis of wood shear walls." *J. Struct. Eng.*, 10.1061/(ASCE)0733-9445(2001)127:4(433), 433–441.

Folz, B., and Filiatrault, A. (2004). "Seismic analysis of woodframe structures. I: Model formulation." *J. Struct. Eng.*, 10.1061/(ASCE)0733-9445(2004)130:9(1353), 1353–1360.

Foschi, R. O. (1977). "Analysis of wood diaphragms and trusses. Part 1: Diaphragms." *Can. J. Civ. Eng.*, 4(3), 345–352.

Gagnon, S., Bilek, E. M., Podesto, L., and Crespell, P. (2013). "Introduction to cross-laminated timber." Chapter 1, *CLT handbook: Cross-laminated timber—US edition*, E. Karacabeyli and B. Douglas, eds., FPInnovations, Pointe-Claire, QC, Canada.

Gagnon, S., and Pirvu, C., eds. (2011). *CLT handbook: Cross-laminated timber*, FPInnovations Program, Pointe-Claire, QC, Canada.

ICC (International Code Council). (2009). "International building code." Washington, DC.

Kircher, C., Reitherman, R., Whitman, R., and Arnold, C. (1997). "Estimation of earthquake losses to buildings." *Earthquake Spectra*, 13(4), 703–720.

Newcombe, M. (2007). "Seismic design of multi-storey post-tensioned timber buildings." Master dissertation, Univ. of Pavia, Pavia, Italy.

NZS (New Zealand Standards). (2006). "Concrete structures standard: Appendix B: Special provisions for seismic design of ductile jointed precast concrete structural systems." *NZS 3101*, Wellington, New Zealand.

Palermo, A. (2004). "Use of controlled rocking in the seismic design of bridges." Ph.D. thesis, Technical Institute of Milan, Milan, Italy.

Palermo, A., Pampanin, S., Buchanan, A., and Newcombe, M. (2005). "Seismic design of multi-storey buildings using laminated veneer lumber (LVL)." *2005 NZSEE Conf.*, New Zealand Society for Earthquake Engineering, Wellington, New Zealand, 8.

Pampanin, S., Priestley, M. J. N., and Sritharan, S. (2001). "Analytical modelling of the seismic behavior of precast concrete frames designed with ductile connections." *J. Earthquake Eng.*, 5(3), 329–367.

Pang, W., Rosowsky, D. V., Pei, S., and van de Lindt, J. W. (2007). "Evolutionary parameter hysteretic model for wood shear walls." *J. Struct. Eng.*, 10.1061/(ASCE)0733-9445(2007)133:8(1118), 1118–1129.

Pang, W., Rosowsky, D. V., Pei, S., and van de Lindt, J. W. (2010). "Simplified direct displacement design of a six-story wood frame building and pre-test performance assessment." *J. Struct. Eng.*, 10.1061/(ASCE)ST.1943-541X.0000181, 813–825.

Pang, W. C., and Rosowsky, D. V. (2010). "Beam-spring model for timber diaphragm and shear walls." *Struct. Build.*, 163(SB4), 227–244.

PCI (Precast/Prestressed Concrete Institute). (2010). "Design aid 15.3.3 typical design stress-strain curve, 7-wire low-relaxation prestressing strand." *PCI (precast/prestressed concrete institute) design handbook*, 7th Ed., Chicago, 15–32.

PEER (Pacific Earthquake Engineering Research Center). (2008). "Pacific earthquake engineering research center: Next generation of ground-motion attenuation models (NGA) database." ⟨http://peer.berkeley.edu/nga/⟩ (Mar. 15, 2008).

Pei, S., and van de Lindt, J. W. (2011a). "Approximate response reduction factor calibration of cross laminated timber walls for mid-rise wood buildings." FPInnovation, Vancouver, Canada.

Pei, S., and van de Lindt, J. W. (2011b). "Seismic numerical modeling of a six-story light-frame wood building: Comparison with experiments." *J. Earthquake Eng.*, 15(6), 924–941.

Pei, S., van de Lindt, J. W., Wehbe, N., and Liu, H. (2013). "Experimental study of collapse limits for wood frame shear walls." *J. Struct. Eng.*, 10.1061/(ASCE)ST.1943-541X.0000730, 1489–1497.

Popovski, M., Schneider, J., and Schweinsteiger, M. (2010). "Lateral load resistance of cross-laminated wood panels." *Proc., 11th World Conf. on Timber Engineering 2010*, Wood Technology Society, Division of the Institute of Material, Minerals and Mining, London.

Priestley, M. J. N. (1991). "Overview of the PRESSS research programme." *PCI J.*, 36(4), 50–57.

Priestley, M. J. N., Sritharan, S., Conley, J. R., and Pampanin, S. (1999). "Preliminary results and conclusions from the PRESSS five-story precast concrete test-building." *PCI J.*, 44(6), 42–67.

Priestley, M. J. N., and Tao, J. R. (1993). "Seismic response of precast prestressed concrete frames with partially bonded tendons." *PCI J.*, 38(1), 58–69.

Shao, X., et al. (2014). "Real-time hybrid simulation of a multi-story wood shear wall with first-story experimental substructure incorporating a rate-dependent seismic energy dissipation device." *Smart Struct. Syst.*, 14(6), 1031–1054.

Vamvatsikos, D., and Cornell, C. A. (2002). "Incremental dynamic analysis." *Earthquake Eng. Struct. Dyn.*, 31(3), 491–514.

Van de Lindt, J. W., Pei, S., Pang, W., and Rosowsky, D. V. (2011). "IDA comparison of IBC-designed and DDD-designed six-story light-frame wood buildings." *J. Perform. Constr. Facil.*, 10.1061/(ASCE)CF.1943-5509.0000150, 138–142.

Van de Lindt, J. W., Rammer, D., Popovski, M., Line, P., Pei, S., and Pryor, S. E. (2013). "Lateral design of cross-laminated timber building." Chapter 4, *CLT handbook: Cross-laminated timber—US edition*, E. Karacabeyli and B. Douglas, eds., FPInnovations, Pointe-Claire, QC, Canada.

Wanninger, F., and Frangi, A. (2014). "Investigation of a post-tensioned timber connection—Test report." Institute of Structural Engineering, Swiss Federal Institute of Technology Zurich, Zurich, Switzerland.

Downloaded from ascelibrary.org by Thang Dao on 09/07/16. Copyright ASCE. For personal use only; all rights reserved.